Observations of Fatigue Crack Behaviour in Proton Irradiated 304 Stainless Steel

R.P.Spencer and E.A.Patterson

School of Engineering, Harrison Hughes Building, University of Liverpool, Liverpool, UK

Abstract

Thermoelastic stress analysis (TSA) has been used to monitor fatigue crack growth in 304 grade austenitic stainless steel compact tension (CT) specimens that have been subject to proton irradiation. Several specimens had a 10x10mm area ahead of a 1mm pre-crack irradiated with a 1.6MeV proton beam up to 0.216C to 0.648C of accumulated charge prior to fatigue testing. Subsequently, specimens were loaded sinusoidally at 20Hz with an R-ratio of 0.5, and TSA data was collected both at the loading frequency and its second harmonic. Irradiation appears to cause an increase in the fatigue life, with a reduction in crack growth rate observed in the irradiated specimens compared to the unirradiated control specimens. Irradiation damage caused an increase in the value of the effective amplitude of the stress intensity factor and a linear change in the parameters of the Paris Law with accumulated charge from the irradiation.

1. Introduction

Austenitic stainless steels are widely employed as structural materials both in-core and out-of-core in light water reactors (LWRs) and in service will experience cyclic loading, associated with temperature changes which occur during power transients, that could cause the growth of sub-critical cracks. Of interest in this study are austenitic steel components that are subject to cyclic loading and radiation damage, with a focus on the effect of this damage on fatigue crack growth behaviour.

Using Linear Elastic Fracture Mechanics (LEFM), Paris & Erdogan proposed that the stress intensity factor, K, is empirically related to crack growth rate [1]:

$$\frac{da}{dN} = C(\Delta K)^m \quad (1)$$

where:a is the crack length, N is the number of cycles, ΔK is the stress intensity factor range and C, m are empirical constants. The sub-critical crack growth experienced by the

component can be modelled by this equation or modifications thereof that consider additional effects such as R-ratio, temperature or loading frequency [2].

Radiation damage causes changes to the mechanical properties of the steel, such as an increase in hardness, transmutation or swelling [3]. The effects of radiation damage on fatigue crack growth are less clear, with a review by James [2] reporting on a number of studies that find that neutron damage increases, decreases or does not change crack growth rate. A study by Margolin et al [4] found that the crack growth rate in neutron-irradiated austenitic steels was more dependent on the swelling than the total damage and that increased swelling caused an increase in the crack growth rate.

Proton irradiation can be used to replicate effects of neutron irradiation. Fenici & Suolang [5] found that proton irradiated austenitic steel was more resistant to crack initiation and has a reduced crack growth rate compared to unirradiated controls when using load-controlled testing. Nogami et al [6] found the opposite behaviour in low-cycle, strain-controlled fatigue testing where proton irradiation reduced the time for crack initiation. Murase et al [7] found an increase in fatigue life due to proton irradiation, as did Shulov & Nochovnaya [8] for metals subject to heavy ion irradiation.

2. Experimental Methods

2.1 Thermoelastic Stress Analysis

Thermoelastic stress analysis (TSA) is a non-contact surface stress measurement technique that uses an infrared camera to correlate the temperature changes of a dynamically-loaded specimen with the change in stress. In order to associate the change in temperature with a change in stress a lock-in procedure to a reference signal must be performed. The reference signal can come from any source that is in-phase with the loading. In practice, this is usually the load-cell or an accelerometer, but recently self-reference algorithms have been developed to allow a region in the field-of-view of the infrared camera to be used to generate a reference signal which, by definition, is in-phase. The data produced by a TSA system is vectorial as each set of data captured has an associated R-image (magnitude) and θ-image (phase measured relative to the forcing signal). These can be equivalently represented by Cartesian transforms to an X-image (in-phase) and Y-image (out-of-phase).

By applying a calibration factor, it is possible to convert the camera units to stress units. The relationship for an isotropic material under biaxial stress at each pixel is given by [9]:

$$AS = \Delta(\sigma_1 + \sigma_2) \quad (2)$$

where: A is the calibration factor, S is the detector signal, and $\sigma_{1,2}$are the principal stresses on the surface. The addition of a region of radiation damage in this work requires a consideration of the underlying factors that contribute to the calibration factor, A, which is comprised of a number of detector-related constants and the thermoelastic parameter K [9] . Wong et al [10] performed a derivation of the thermoelastic parameter taking into account the effect of mean load; and this introduces terms relevant to the effects of radiation damage. The thermoelastic parameter of Wong et al is given by:

$$K = \left(\alpha - \frac{1}{E^2}\frac{\partial E}{\partial T} s_m\right)(\rho_o C_\varepsilon)^{-1} \quad (3)$$

where: α is the coefficient of thermal expansion, E is the modulus of elasticity, T is the absolute temperature, s_m is the mean stress, ρ_o is the material density and C_ε the heat capacity at constant strain. Early studies by Charlesby et al [11] on the change in elastic modulus of austenitic steels with exposure to radiation found a change of no more than 0.3%. The density will change if irradiation swelling is significant; however, at the low level of damage used in this study, volumetric changes due to swelling are unlikely. Limited data is available on the effects of radiation damage on the coefficient of thermal expansion; but, the low level of damage used should limit the variation. Therefore, radiation damage should have little effect on the magnitude of the thermoelastic parameter K.

Calibration of the system is performed by capturing TSA data from a region of uniform uniaxial stress, typically in a middle tension (MT) specimen subject to cyclic loading. The stress amplitude applied to the specimen is calculated and then used to determine the factor A in MPa$\sqrt{\text{m}}$ / Camera unit.

Once calibrated, a multi-point overdeterministic method can be used to fit a Muskhelishvili-type stress distribution [12] to the singularity-dominated stress field ahead of the crack tip; and hence, to obtain the amplitude of the effective stress intensity factor ΔK_{eff} from the X-image as described by Diaz et al [13]. In this work, the FATCAT [14] software (*http://www.experimentalstress.com/software.htm*) has been used to perform this procedure.

By locating the crack tip in each image, TSA data can be used to monitor crack length during a fatigue test [15]. The feature typically used as a first approximation of the crack tip in TSA data was identified Diaz et al [13] as the point where the phase angle, along the path of the crack, changes sign. An improved estimate of the crack tip location is provided by fitting the Muskhelishvili-type stress distribution to the TSA data using FATCAT and taking the position of the crack tip as an unknown.

In order to produce a uniform and high signal in the infrared spectrum, the surface of the specimen requires coating. The emissivity of the bare metal is typically ~0.3 and produces poor thermoelastic data. A paint or a graphite coating is required to increase the emissivity, but must be thin to avoid masking the thermal signal from the underlying metal.

2.2 Specimen Design & Material

In this study, thin-gauge compact tension specimens were used. Their design followed ASTM-E647 [16], but was thinner than the standard at 0.8mm. This was required to fit them in the end-station of the accelerator, as described in the following section. The validity of thin-gauge austenitic stainless steel specimens in fatigue tests has been previous established by Rickerby & Fenici [17]. Table 1 shows the elemental composition of the 304 stainless used.

Following manufacture, the surface to be imaged on each of the specimens was ground and polished, finishing with a 40nm colloidal silica polish. Prior to fatigue testing a graphite coating was applied in the form of Graphit33 spray (*Kontakt Chemie*). This increased the surface infrared emissivity from ~0.3 to ~0.9. The specimens were pre-cracked to a length of nominally 4mm using a constant R-ratio decreasing sinusoidal load, beginning with 600N ± 200N ending with of 450N ± 150N at 80Hz, decreasing in steps of 10N in amplitude and 30N in mean load, with 30,000 cycles at each load level. The graphite coating was removed using ethanol prior to irradiation and reapplied before fatigue testing.

2.3 Proton Irradiation

Proton irradiation is often used as a surrogate for neutron irradiation. The advantage of proton irradiation is in the ability to control dose rate, total dose, temperature, and a lower level of activation. However, the interactions between incident protons and the target are different to those of neutrons due to the charge of the proton. In order to replicate some features of neutron damage at reactor temperatures (~290˚C), a higher proton irradiation temperature must be used. For example, Was & Allen [18] suggest a temperature of 360-400˚C to replicate the effects of radiation-induced segregation, such as chromium depletion.

Accelerator

All irradiations were performed at the Dalton Cumbrian Facility (DCF) [19] using the ‘Baby’ 2.5MV single-ended accelerator (National Electrostatics Corporation, *Wisconsin, USA)* which can produce a high current (~100μA) proton beam. The protons are generated by a radio frequency plasma source located inside the high voltage terminal. Beam shape and focus were checked by beam position monitors and controlled by a series of Einzel lenses and

magnetic quadrupoles located at various points along the beamline. This resulted in a beam with a circular spot approximately 2mm in diameter, with a Gaussian intensity profile. The shape of the irradiated area was controlled by a set of four moveable tantalum vanes. During irradiation, the beam was rastered over the vanes resulting in a sharp, square irradiated area.

Temperature control/target stage

The target stage used for this experiment was of a similar design to that described by Wady et al [19]. It was located at the end of a beamline in a vessel that could be isolated from the beamline and be restored to atmospheric pressure to allow for specimen mounting.

The stage consisted of a cooling loop through a nickel block containing 3 cartridge heaters. Upon this was mounted an indium shim, followed by a ceramic heater, a further indium shim and finally the specimen, which was held in place by a stainless steel plate and surrounded by a tantalum shield. The indium shims melted during operation and provided good thermal contact between the specimen, heater and cooling loop.

On top of the tantalum shield was mounted an array of scintillator slides, with marks to indicate the planned irradiation area. During beam alignment, a low current beam with a wide raster was used and the vanes moved such that the scintillator glow matched the prepared marks.

A thermocouple was spot-welded to the specimen to allow calibration of an infrared camera that observed the specimen during irradiation. In this way, the temperature of the specimen could be monitored during the test and the power of the heater varied, if required, to maintain the desired temperature.

The beam current was monitored during the irradiation by measuring the current hitting the target stage using a nano-ammeter. Current could be altered by varying the raster size or modifying the plasma source parameters. The total dose to the specimen was calculated by integrating the beam current over time to determine the total charge deposited during the experiment.

Proton activations

Though generally understood to create a lower activation than neutron irradiations, there was still activation from proton irradiation. Of particular difficulty with iron-based alloy proton irradiations is the production of Co^{57} by the $Fe^{56}(p,\gamma)Co^{57}$ interaction. Co^{57} has a half-life of

271.74d [20], and would result in an extended cooling period to allow the activity to decay to safe levels for handling.

Between 2 to 3MeV the production cross-section of Co^{57} increases from <100μb to >1mb [21]. Hence, a beam energy of 1.6MeV was chosen to limit the production of Co^{57} in the specimen. This resulted in a cooling period of between 6 and 12 weeks, depending on the irradiation time.

Damage Profile

In order to estimate the radiation damage to the specimens and the amount of deposited hydrogen, a Monte-Carlo simulation of the ion interactions was performed using the Stopping Range of Ions in Matter (SRIM) software [22]. Following the best practice advised by Stoller at al [23], SRIM was used in the Kinchin-Pease quick calculation setting with a displacement energy of 40eV and a binding energy of 0eV for the target atoms. Radiation damage, was then calculated from the NRT model [24], which calculates the amount of atomic displacements produced by an incident particle of a given energy, using outputs from SRIM [23].

Figure 1 shows the profile of damage with depth caused by proton irradiation with an accumulated charge of 0.216C, which is approximately constant at 0.07 – 0.1 DPA to a depth of about 10μm where a sharp peak of 1 DPA occurs with no damage beyond 15μm. The shape of the curve in Figure 1 corresponds to the well-known Bragg curve that describes the specific energy loss of a charged particle as a function of penetration into a media, with the peak at about 13μm being known as the Bragg peak.

The damage profile is highly non-uniform and occurs in a surface layer of approximately 13μm, leaving the bulk of the material unaffected. This results in some difficulty quantifying the damage level, as the Bragg peak damage is many times higher than the uniform region. In general, thermoelastic stress analysis is only sensitive to changes in surface stresses, and so will only detect changes in behaviour resulting from the radiation damage. Table 2 shows information related to the irradiation of each specimen.

Implanted Hydrogen

The results from the SRIM calculations for irradiation with an accumulated charge of 0.216C are shown in figure 1 and indicate that the level of hydrogen deposited in the specimen is high, many orders of magnitude higher than the values used for hydrogen embrittlement tests. However, it is not clear how much hydrogen is retained, as the diffusivity of hydrogen

in austenitic steels is high [26], although irradiation-induced defects act as traps for diffusing hydrogen [27].

Irradiation Location

Due to the mounting and geometry of the specimen, it was not feasible to irradiate the whole specimen surface. An area of 10x10mm was irradiated using a rastered beam, 4.5mm from the load line (1.5mm from the notch tip) and symmetrically arranged around the axis of symmetry through the notch. This area was ahead of the fatigue pre-crack, to prevent indium ingress into the crack from the shim and was much larger than the anticipated size of the plastic zone at the crack tip as well as being larger than the field-of-view of the TSA system. The location also allowed observation of crack growth during the transition from virgin material into damaged material and the effect of damage gradients.

2.4. Testing Program

Prior to irradiation, the specimens were precracked to a crack length of ~4mm as per ASTM E647 [16].

The irradiation procedure was as follows:

1. The specimen was mounted in the target stage, as described above, and the end-station pumped to a high vacuum (~1x 10^{-7} Torr).

2. The target stage was heated to the proposed irradiation temperature and the IR camera calibrated.

3. The beam transmission and alignment were optimised. The tantalum vanes were positioned to ensure the required area was irradiated using a low current beam.

4. The beam current was increased to the required level and the specimen heating adjusted to compensate for the heating due to the beam.

5. The specimen was irradiated until the required charge accumulated. The beam current, specimen temperature and accumulated charge were monitored and the settings changed, as necessary, to ensure consistency over the duration of the irradiation.

Following irradiation, the specimens were tested using a constant amplitude of load in a tensile test machine (*Electropuls E3000, Instron*). A 20Hz sinusoidal load was applied with mean load of 450N and amplitude of 150N, with an R-ratio of 0.5. All tests were conducted in ambient laboratory conditions.

During the fatigue tests, the crack growth was monitored using an infrared camera (*SC7650 InSb, FLIR*) networked with a PC running DeltaTherm2 (*StressPhotonics, Maddison, WI*) to perform TSA. The camera was aligned such that the left edge of the field-of-view was located at tip the machined notch; and therefore, crack length could be easily calculated by scaling the pixel position of the crack tip, where 1 pixel = 0.033mm. DeltaTherm2 allows the user to collect TSA data at the loading frequency (first harmonic) and at double the loading frequency (second harmonic). The crack growth rate was calculated from the crack lengths determined by the stress-distribution fit procedure using the incremental polynomial methodology outlined in Appendix XI of ASTM E647 [16].

Following fatigue testing, microhardness measurements were made across the surface of specimens parallel to the crack to locate the edge of the irradiation damage. The increase in hardness due to the radiation damage was modelled using a logistic curve, of the form:

$$H(x) = H_0 + \frac{H_I}{e^{-s(x-x_I)}} \tag{4}$$

where: H is the hardness, x is the distance from the load line, H_0 the hardness of the unirradiated region, H_I the increase in hardness due to the radiation damage, s is the sharpness of the transition and x_I the location of the midpoint of the hardness transition. The length x has been chosen such that it has the same basis as the crack length.

3. Results & Discussion

An example of the fit of the model given in Equation (4) is shown in Figure 2. Microhardness data for each specimen is presented in Table 3 and shows that the hardness increase, H_I increased linearly ($R^2 = 0.93$) with the irradiation damage measured by the accumulated charge. The location of the midpoint, x_I, has been taken to be the edge of the irradiation damage. This was planned to be at x_I =4.5mm and it was within 0.3mm of this value in all specimens. A crack length of 5mm can be therefore assumed to be fully within the irradiated material for all specimens.

Figure 3 shows that radiation damage causes an increase in total fatigue life of the specimens; although specimen I2.A, which was subject to irradiation with an accumulated charge of 0216C, is an outlier because its crack grew more slowly than the crack in the specimens that received accumulated charges of 0.432C or 0.648C. This will be discussed in more detail below. The overall increase in fatigue life with proton irradiation is in agreement with the results of Murase et al [7] and of Shulov & Nochovnaya [8].

The crack growth rate as a function of crack length is shown in figure 4 for both the irradiated and unirradiated specimens and it is clear that the crack growth rate is consistently lower for the irradiated specimens which is consistent with findings of Fenici & Suolang [5]. This appears to be caused by a shallower gradient at the start of the fatigue test as the crack tip progresses across the boundary between the unirradiated and irradiated material, i.e. at crack lengths between 4.5mm and 5mm long. Once the crack tip and its process zone are fully within the irradiated material, the gradient of the curves is more similar to the value for the unirradiated specimens. Specimen I2.A, which exhibited the anomalous behaviour in figure 3, and specimen I6.A, which received an accumulated charge of 0.648C, have an almost constant crack growth rate for the first half millimeter of crack length. The monitored data from the accelerator were examined in detail for these specimens, which were irradiated in the same session at the accelerator facility, and it was found that they had been subjected to a short temperature excursion from the planned 360°C to 480°C and 440°C respectively prior to being irradiated. This occurred due to a temporary loss of control of the heating system caused by solidification of part of the Indium shim which reduced thermal contact with the specimen. The values for the hardness in the unirradiated regions of these specimens are 10% higher than for the other irradiated specimens (see Table 3). Hence, these short excursions to an elevated temperature might have induced a rise in the base hardness and a corresponding increase in the modulus of elasticity, which would have increased the constraint on the plastic zones ahead and behind the pre-crack due to a reduction in the stiffness and deformation of the surrounding elastic material. And, in turn, this might have caused a closure effect to be induced. In addition, or alternatively, it is possible that this resulted in some Indium becoming jammed in the pre-crack and could have been responsible for a crack closure mechanism operating at the start of the post-irradiation fatigue test, which would account for the initial constant rate of crack growth.

Figure 5 shows the amplitude of the effective stress intensity factor, ΔK_{eff}, obtained by fitting stress field equations to the field of TSA data, as a function of the crack length. The separation of data from the irradiated and unirradiated specimens is less distinct than for the crack growth rate; nevertheless, the values for effective stress intensity of the irradiated specimens are generally higher than for the unirradiated specimens. Again, specimen I2.A exhibits anomalous behaviour with an almost constant value of ΔK_{eff} for the initial millimetre of crack growth after the irradiation, which would be consistent with a flank closure mechanism. Similar, but less distinct, behaviour is exhibited by specimen I6.A over the same crack length, i.e. from 4 to 5 mm. Further evidence of the presence of closure in specimen I2.A is provided in figure 6 which shows a comparison of TSA data captured at a crack length of 4.64mm for this specimen and an unirradiated one. The maps of the

magnitude of the TSA signal at the same frequency as the load cycle are similar for both specimens, indicating similar values for ΔK_{eff}. However, the maps of the magnitude of the second harmonic of thermoelastic signal are different, with a strong signal present along the crack flanks in the irradiated specimen, which has been associated with closure by Palumbo et al [28], while there is no signal in the unirradiated specimen. This distribution of the magnitude of the second harmonic of the TSA data was also detected in specimen I6.A which had also been subjected to the short-term temperature excursion in the accelerator prior to irradiation; but was not observed in the unirradiated specimens or the other irradiated specimens. Thus, it seems reasonable to conclude that the anomalous behaviour observed in specimen I2.A and to a lesser extent in specimen I6.A was due to a closure mechanism introduced accidently during the process of irradiation.

Plots of the Paris law relationship are shown figure 7 for all of the specimens, i.e. crack growth rate as a function of the amplitude of the effective stress intensity factor, ΔK_{eff}, and show that generally the irradiated specimens have a lower crack growth rate than the unirradiated controls. The Paris law in equation (1) was fitted to the data in figure 7 for each specimen and the results are tabulated in Table 4. The fit has been performed in two regimes: for the complete post-irradiation fatigue test; and for the data acquired when the crack tip was beyond the edge of the irradiated zone, as indicated by the hardness data in Table 3, i.e. for crack lengths greater than 5mm. Figure 8 shows the latter data from table 4 graphically with data from the outlier, specimen I2.A, removed and there is linear correlation of the Paris law coefficient, m with accumulated charge $(R^2 = 0.91)$ and an inverse linear correlation of logarithm of the Paris law coefficient, $\log C$ with accumulated charge $(R^2 = 0.93)$.

These concurrent changes in the Paris Law coefficients suggest that the irradiation is causing an initial reduction in the crack growth rate, but an increase in crack growth rate at larger values of the amplitude of the effective stress intensity factor, ΔK_{eff}. This implies there will be an intersection point for the curves for an unirradiated and an irradiated specimen beyond which the crack rate of the irradiated material will exceed that of the unirradiated material. For example, beyond $\Delta K_{eff} = 23\mathrm{MPa}\sqrt{\mathrm{m}}$, the increase in crack growth rate of specimen I4.A, which has been irradiated with an accumulated charge of 0.432C, will exceed that of the unirradiated specimen U.A. This suggests that for shorter cracks, the reduced crack growth rate observed in irradiated specimens, is protective; but at longer crack lengths and hence higher amplitude of stress intensity, the crack growth rate may accelerate. These observations and those concerning the behaviour of cracks traversing a boundary or gradient in radiation damage are important because real components are

unlikely to be irradiated in a perfectly uniform manner over their length [29] or through their thickness [30].

5. Conclusions

Compact tension specimens of 304 stainless steel with a pre-crack have been subjected to increasing levels of radiation damage, from accelerated protons, in an area ahead of the pre-crack. Post-irradiation fatigue testing shows that irradiation caused a reduction in crack growth rate and a small increase in the amplitude of the effective stress intensity factor measured using thermoelastic stress analysis. When the Paris law was fitted to the data for crack growth within the irradiated region, it was found than there was a linear correlation between the level of irradiation represented by the accumulated charge and the coefficient, m representing the gradient of the Paris curve, but an inverse linear correlation with $\log C$, where C is the intercept of the linear portion of the Paris curve with the crack growth rate axis.

The rate of change of crack growth rate in irradiated specimens was slower than in unirradiated specimens while the crack tip was traversing the boundary between unirradiated and irradiated material. In two specimens, the crack growth rate was constant over a crack extension of about 0.5mm as the crack tip propagated into the irradiated region and this appears to have been associated with crack closure, as indicated by a reduction in ΔK_{eff} and the presence of signals caused by crack flank contact in the second harmonic data from thermoelastic stress analysis. This behaviour is believed to have been a consequence of unplanned events during setting up for the irradiation in the accelerator.

The effects of irradiation have been observed despite the relatively shallow depth of the damage (15μm) compared to the specimen thickness (800μm) and have been demonstrated to be significant to fatigue crack growth with all irradiated specimens having a fatigue life that was longer than the unirradiated specimens.

Acknowledgements

RPS was supported jointly by the EPSRC Next Generation Nuclear CDT and Rolls-Royce. We acknowledge the support of the Dalton Cumbrian Facility (DCF), the experimental base of The University of Manchester's Dalton Nuclear Institute and a partner in the National Nuclear User Facility, the EPSRC UK National Ion Beam Centre and the Henry Royce

Institute. We recognise Samir de Moraes Shubeita for their assistance during the irradiations.
Industrial supervision of RPS was provided by Dr Nick Riddle, Dr Daniel Cogswell and Dr Keith Wilford and many detailed discussions with them are gratefully acknowledged.

References

[1] P. Paris and F. Erdogan, “A Critical Analysis of Crack Propagation Laws,” *J. Basic Eng.*, vol. 85, no. 4, p. 528, 1963.

[2] L. A. James, “Fatigue Crack Propagation in Austenitic Stainless Steels,” *At. Energy Rev.*, vol. 14, no. 1, pp. 37–86, 1976.

[3] F. A. Garner, “Radiation Damage in Austenitic Steels,” in *Comprehensive Nuclear Materials*, Elsevier, 2012, pp. 33–95.

[4] B. Margolin, A. Minkin, V. Smirnov, A. Sorokin, V. Shvetsova, and V. Potapova, “The radiation swelling effect on fracture properties and fracture mechanisms of irradiated austenitic steels. Part II. Fatigue crack growth rate,” *J. Nucl. Mater.*, vol. 480, pp. 15–24, 2016.

[5] P. Fenici and S. Suolang, “Fatigue crack growth in 316 type stainless steel at temperatures and displacement damage rates representative for the first wall loading,” *J. Nucl. Mater.*, vol. 194, pp. 1408–1412, 1992.

[6] S. Nogami, Y. Sato, and A. Hasegawa, “Fatigue Crack Initiation in Proton-Irradiated Austenitic Stainless Steel,” *J. Nucl. Sci. Technol.*, vol. 48, no. 9, pp. 1265–1271, 2011.

[7] Y. Murase, J. Nagakawa, and N. Yamamoto, “In-beam fatigue behavior of 20% cold-worked 316 stainless steel at 300 °C,” *Fusion Eng. Des.*, vol. 81, no. 8–14 PART B, pp. 999–1003, 2006.

[8] V. A. Shulov and N. A. Nochovnaya, “Fatigue strength of metals and alloys modified by ion beams,” *Surf. Coatings Technol.*, vol. 158–159, pp. 33–41, 2002.

[9] J. M. Dulieu-Barton, “Introduction to thermoelastic stress analysis,” *Strain*, vol. 35, no. 2, pp. 35–39, 1999.

[10] A. K. Wong, R. Jones, and J. G. Sparrow, “Thermoelastic constant or thermoelastic parameter?,” *J. Phys. Chem. Solids*, vol. 48, no. 8, pp. 749–753, 1987.

[11] A. Charlesby, N. H. Hancock, and H. C. Sansom, “Effect of atomic-pile radiation on the elastic modulus of an austenitic steel,” *J. Nucl. Energy*, vol. 1, pp. 264–273, 1955.

[12] R. A. Tomlinson, A. D. Nurse, and E. A. Patterson, “On Determining Stress Intensity Factors For Mixed Mode Cracks From Thermoelastic Data,” *Fatigue Fract. Eng. Mater. Struct.*, vol. 20, no. 2, pp. 217–226, 1997.

[13] F. A. Diaz, J. R. Yates, and E. A. Patterson, “Some improvements in the analysis of fatigue cracks using thermoelasticity,” *Int. J. Fatigue*, vol. 26, no. 4, pp. 365–376, 2004.

[14] F. A. Díaz, E. A. Patterson, and J. R. Yates, “Application of thermoelastic stress analysis for the experimental evaluation of the effective stress intensity factor,” *Frat. ed Integrità Strutt.*, vol. 25322125, no. 1016, pp. 109–116, 2013.

[15] F. Ancona, R. De Finis, D. Palumbo, and U. Galietti, “Crack Growth Monitoring in Stainless Steels by Means of TSA Technique,” *Procedia Eng.*, vol. 109, pp. 89–96, 2015.

[16] ASTM, “E-647 Standard Test Method for Measurement of Fatigue Crack Growth Rates,” no. July, pp. 1–43, 1999.

[17] D. G. Rickerby and P. Fenici, “Fatigue crack growth in thin section type 316 stainless steel,” *Eng. Fract. Mech.*, vol. 19, no. 4, pp. 585–599, 1984.

[18] G. S. Was and T. Allen, “Intercomparison of microchemical evolution under various types of particle irradiation,” *J. Nucl. Mater.*, vol. 205, pp. 332–338, 1993.

[19] P. T. Wady, A. Draude, S. M. Shubeita, A. D. Smith, N. Mason, S. M. Pimblott, and E. Jimenez-Melero, “Accelerated radiation damage test facility using a 5MV tandem ion accelerator,” *Nucl. Instruments Methods Phys. Res. Sect. A Accel. Spectrometers, Detect. Assoc. Equip.*, vol. 806, pp. 109–116, 2016.

[20] IAEA, “IAEA Chart of Nuclides.” [Online]. Available: https://www-nds.iaea.org/relnsd/vcharthtml/VChartHTML.html.

[21] N. Soppera, E. Dupont, and M. Bossant, *JANIS Book of proton-induced cross-sections*. OECD NEA Data Bank, 2012.

[22] J. F. Ziegler, M. D. Ziegler, and J. P. Biersack, “SRIM - The stopping and range of ions in matter (2010),” *Nucl. Instruments Methods Phys. Res. Sect. B Beam Interact. with Mater. Atoms*, vol. 268, no. 11–12, pp. 1818–1823, 2010.

[23] R. E. Stoller, M. B. Toloczko, G. S. Was, A. G. Certain, S. Dwaraknath, and F. A. Garner, “On the use of SRIM for computing radiation damage exposure,” *Nucl. Instruments Methods Phys. Res. Sect. B Beam Interact. with Mater. Atoms*, vol. 310, pp. 75–80, 2013.

[24] M. J. Norgett, M. T. Robinson, and I. M. Torrens, “A proposed method of calculating

displacement dose rates," *Nucl. Eng. Des.*, vol. 33, no. 1, pp. 50–54, 1975.

[25] H.-H. Jin, S. S. Hwang, M. J. Choi, G. Lee, and J. Kwon, "Proton irradiation for radiation-induced changes in microstructures and mechanical properties of austenitic stainless steel," *J. Nucl. Mater.*, vol. 513, pp. 271–281, 2019.

[26] Y. Murakami and S. Matsuoka, "Effect of hydrogen on fatigue crack growth of metals," *Eng. Fract. Mech.*, vol. 77, no. 11, pp. 1926–1940, 2010.

[27] T. Kato, K. Nakata, J. Kuniya, S. Ohnuki, and H. Takahashi, "Cavity Formation by Hydrogen Injection in Electron-Irradiated Austenitic Stainless Steel," *J. Nucl. Mater.*, vol. 155–157, pp. 856–860, 1988.

[28] D. Palumbo, R. De Finis, F. Ancona, and U. Galietti, "Damage monitoring in fracture mechanics by evaluation of the heat dissipated in the cyclic plastic zone ahead of the crack tip with thermal measurements," *Eng. Fract. Mech.*, vol. 181, pp. 65–76, 2017.

[29] D. W. Sandusky, P. J. Ring, and R. T. Penrose, "Fast Neutron Damage in Type-304 Stainless Steel and High-Nickel Alloys," No. GEAP-13738. General Electric Co., Sunnyvale, Calif. Breeder Reactor Dept., 1971.

[30] I. Remec, "Study of the Neutron Flux and Dpa Attenuation in the Reactor Pressure-Vessel wall," No. ORNL/NRC/LTR-99/5. Oak Ridge National Lab., TN (US), 1999.

Tables

Table 1 - Elemental composition of 304 austenic stainless steel used in experiments.

Element	C	Si	Mn	P	S	Cr	Mo	Ni	Cu	Fe
Wt%	0.03	0.46	1.82	0.018	0.003	18.38	0.27	8.09	0.19	Base

Table 2 – Irradiation and damage parameters for each specimen.

Specimen	Accumlated Charge (C)	Irradiation Time (hrs)	Ion Fluence (ions/cm^2)	Av. Beam Current (A)	Beam Energy (MeV)	DPA Bragg Peak (13.2um)	Average Irradiation Temperature (^{o}C)
U.A		0					
U.B		0					
U.C		0					
I2.A	0.216	4.97	1.35×10^{18}	1.23×10^{-5}	1.6	0.94	347.7
I2.B	0.216	2.86	1.35×10^{18}	2.71×10^{-5}	1.6	0.94	334.1
I4.A	0.432	4.61	2.70×10^{18}	2.61×10^{-5}	1.6	1.87	351.1
I4.B	0.432	4.11	2.70×10^{18}	2.96×10^{-5}	1.6	1.87	360.3
I6.A	0.648	6.29	4.05×10^{18}	2.86×10^{-5}	1.6	2.81	350.4

Table 3 - Hardness parameters from Equation (4) for irradiated specimens.

Specimen	Accumulated Charge (C)	H_0, Base Hardness (HV0.2)	H_I, Hardness Increase (HV0.2)	s Increase sharpness	x_I Midpoint of Increase (mm)
I2.A	0.216	176	15	11	4.49
I2.B	0.216	179	17	64	4.70
I4.A	0.432	164	33	110	4.39
I4.B	0.432	161	40	4	4.88
I6.A	0.648	179	48	12	4.86

Table 4 – Paris Law Parameters for equation (1) for all specimens.

	Fit to all data			*Fit to data from a=5mm*		
Specimen	m	C	R^2	m	C	R^2
U.A	5.16	5.65 x10^{-12}	0.9352	4.27	9.76 x10^{-11}	0.8692
U.B	4.30	9.96 x10^{-11}	0.9601	4.26	1.17 x10^{-10}	0.9538
U.C	4.81	2.41 x10^{-11}	0.9711	4.63	4.13 x10^{-11}	0.9775
I2.A	7.19	1.59 x10^{-14}	0.9595	6.17	3.17 x10^{-13}	0.9933
I2.B	5.08	3.80 x10^{-11}	0.9023	5.08	6.31 x10^{-12}	0.9190
I4.A	4.59	2.94 x10^{-11}	0.8927	5.37	3.16 x10^{-12}	0.9053
I4.B	4.40	5.41 x10^{-11}	0.9542	5.16	5.65 x10^{-12}	0.9839
I6.A	6.89	2.88 x10^{-14}	0.9756	6.00	3.95 x10^{-13}	0.9583

Figures

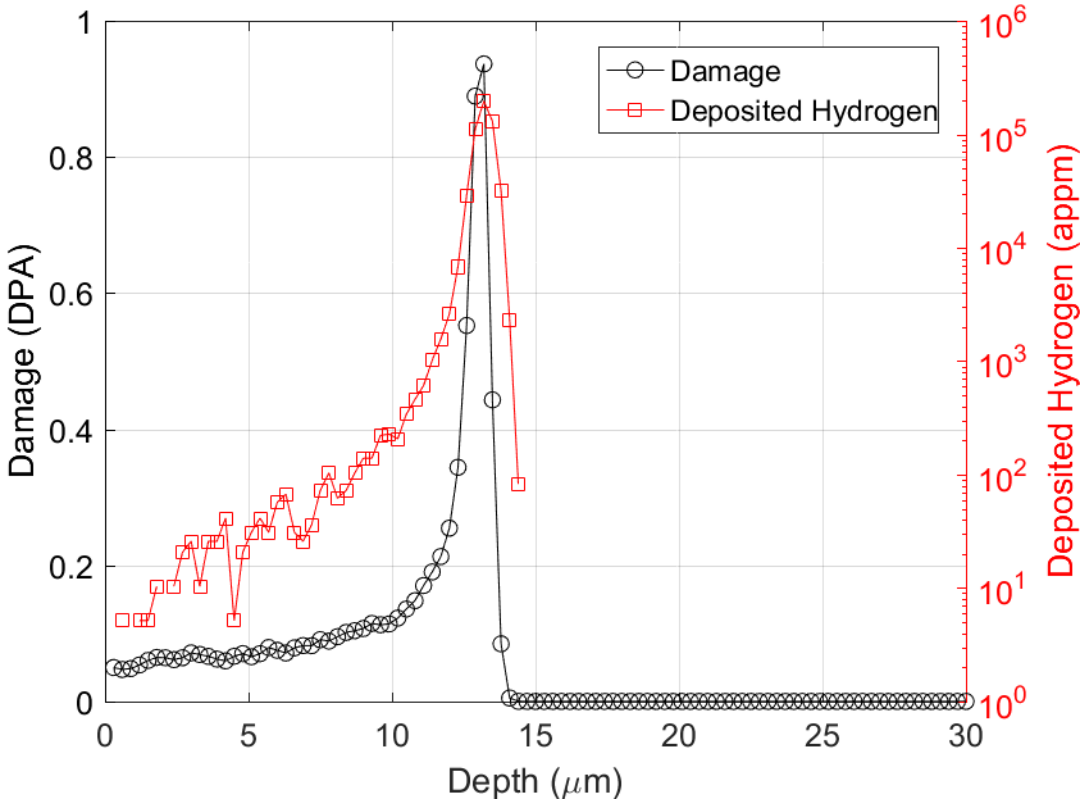

Figure 1 – Calculation, using SRIM, of damage profile (left axis) and deposited hydrogen (right axis) as function of depth.

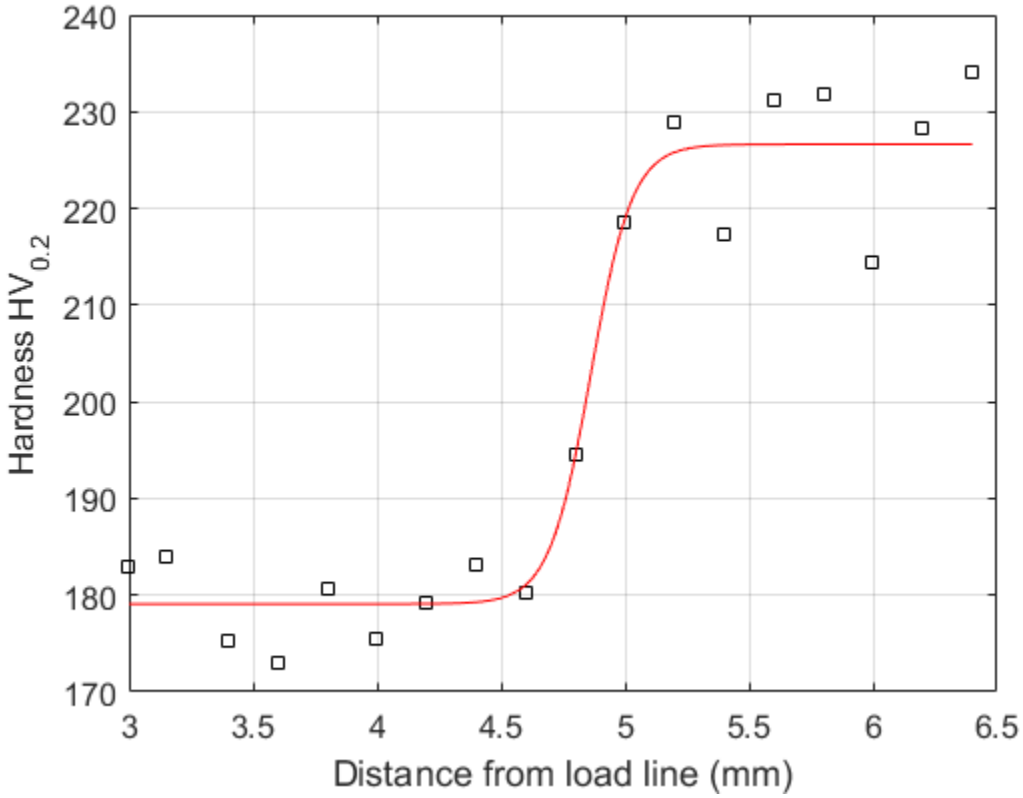

Figure 2 – Distribution of hardness in specimen I6.A which was subjected to irradiation by an accumulated charge of 0.648C; the fit to the data was performed using Equation (4) and the resultant parameters for all specimens are given in Table 3.

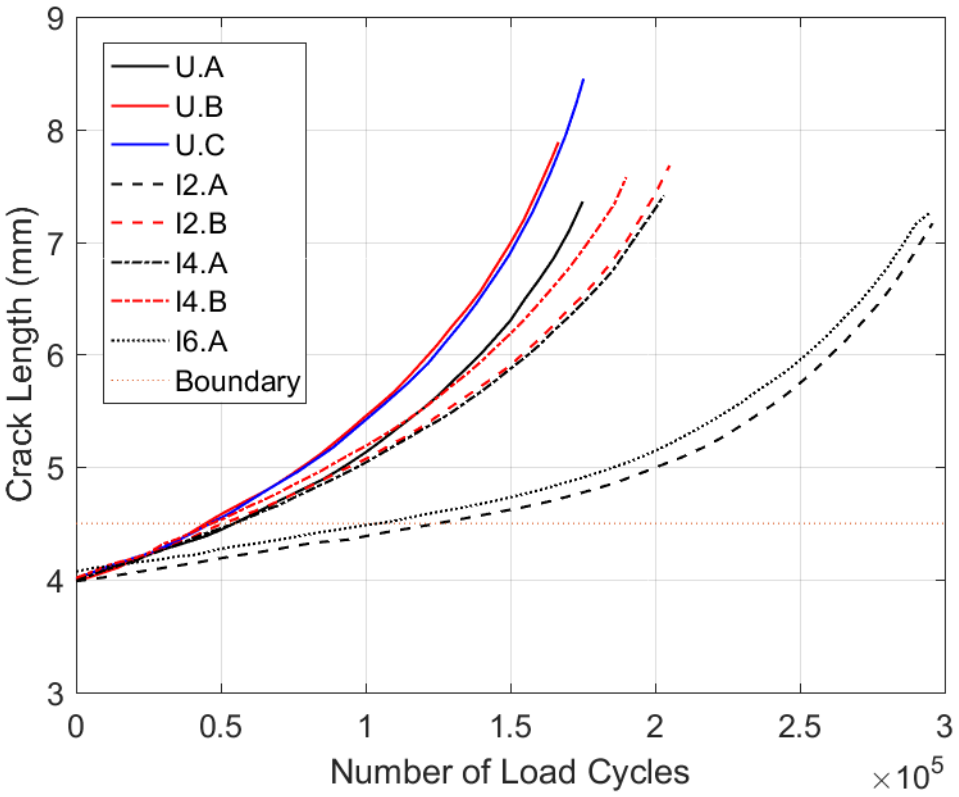

Figure 3 – Crack length as a function of number of load cycles for the post-irradiation fatigue tests starting from a pre-crack of nominal length 4mm that was grown before the irradiation whose nominal boundary is indicated; details of the specimens are provided in table 2.

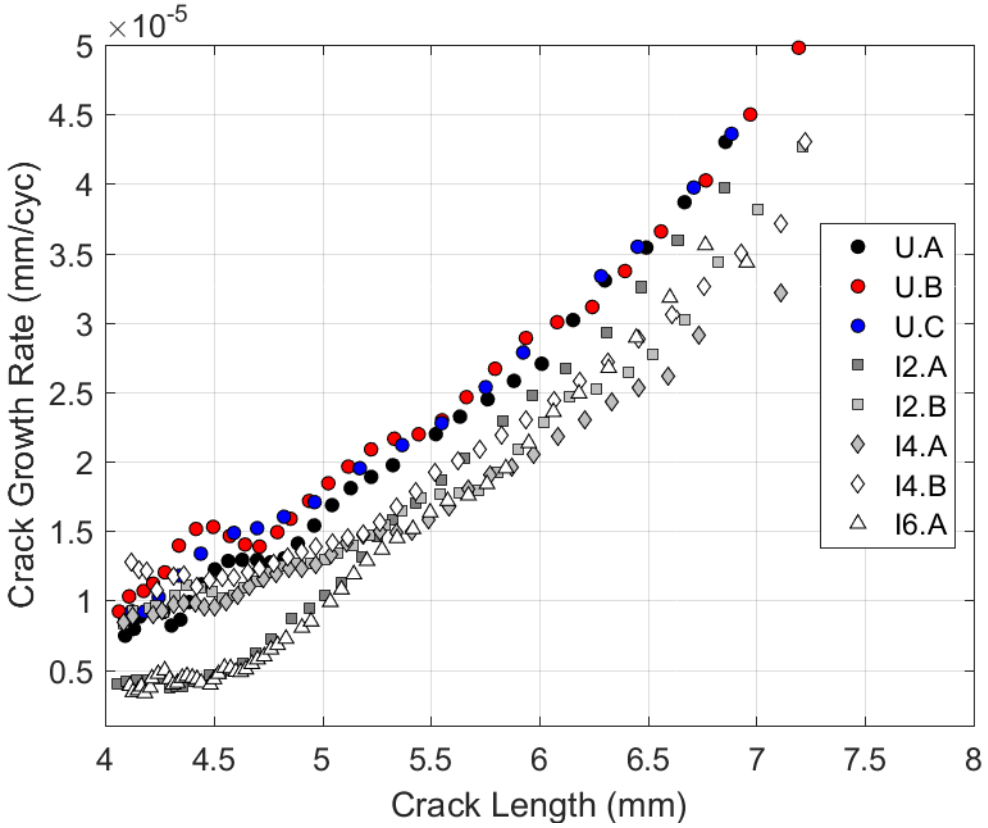

Figure 4 – Crack growth rate as function of crack length for unirradiated (filled circles) and irradiated specimens with a pre-crack; details of the irradiation experienced by each specimen are provided in table 2.

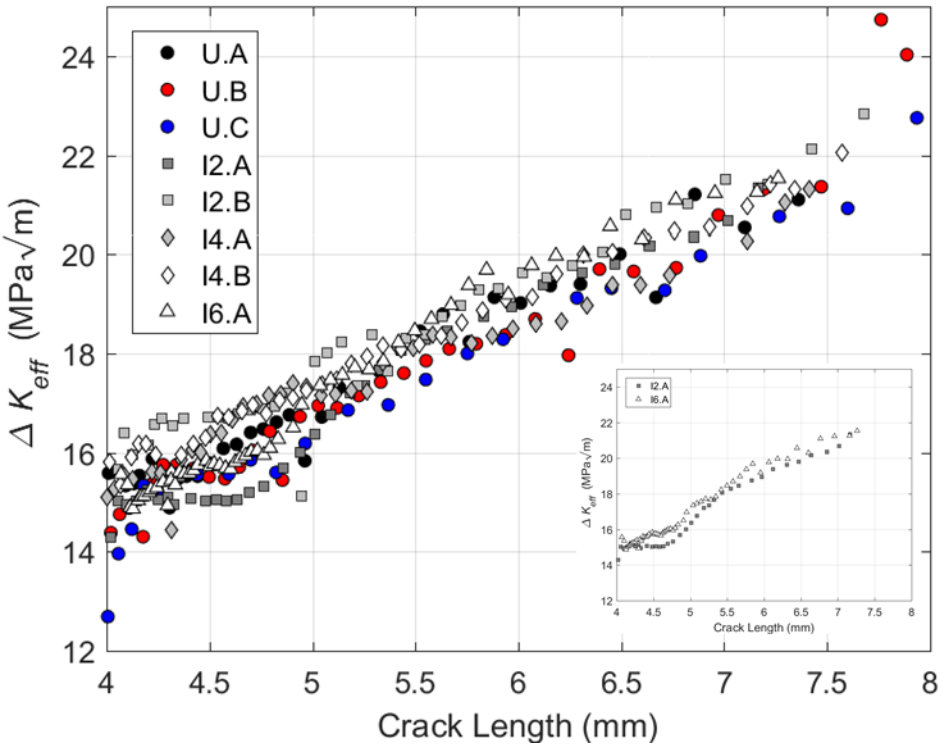

Figure 5 – Amplitude of effective stress intensity factor, ΔK_{eff} as a function of crack length with inset showing data for specimens I2.A and I6.A which accidently experienced a short temperature excursion prior to irradiation in the accelerator.

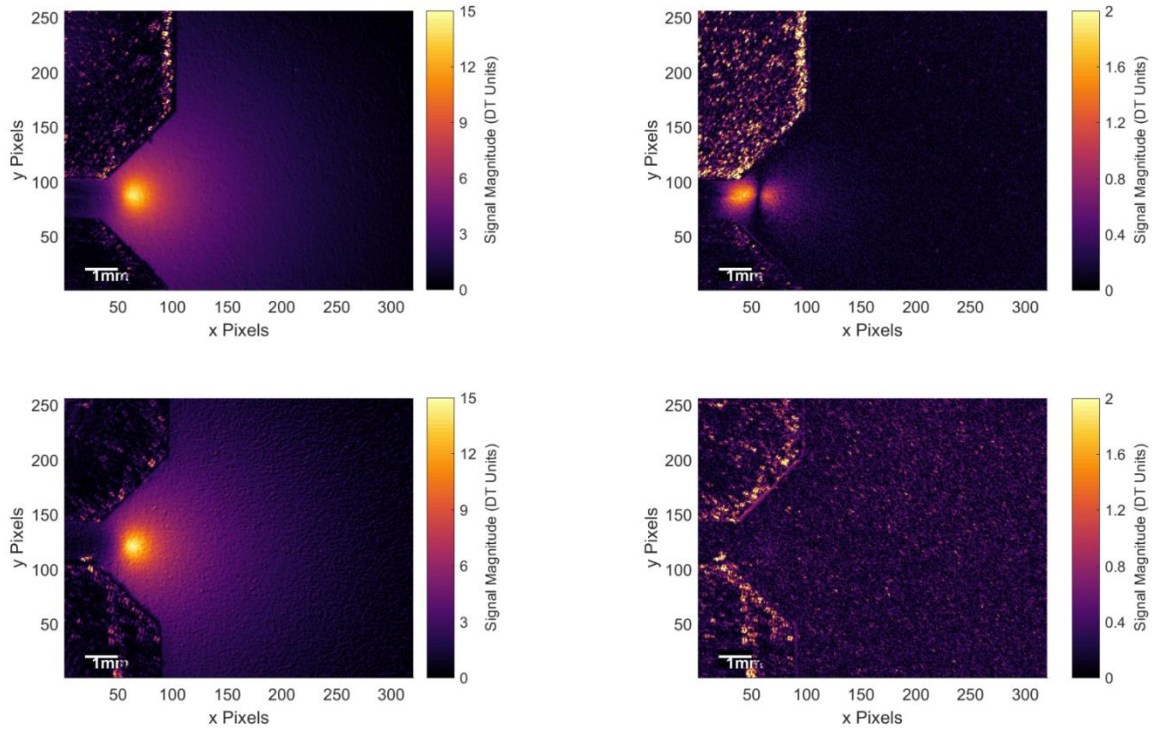

Figure 6 – Maps of the magnitude of the TSA signal (left) and the magnitude of its second harmonic (right) for specimens I2.A (top) and U.B (bottom), which both have a crack of length 4.64mm crack and were subject to the same loading conditions.

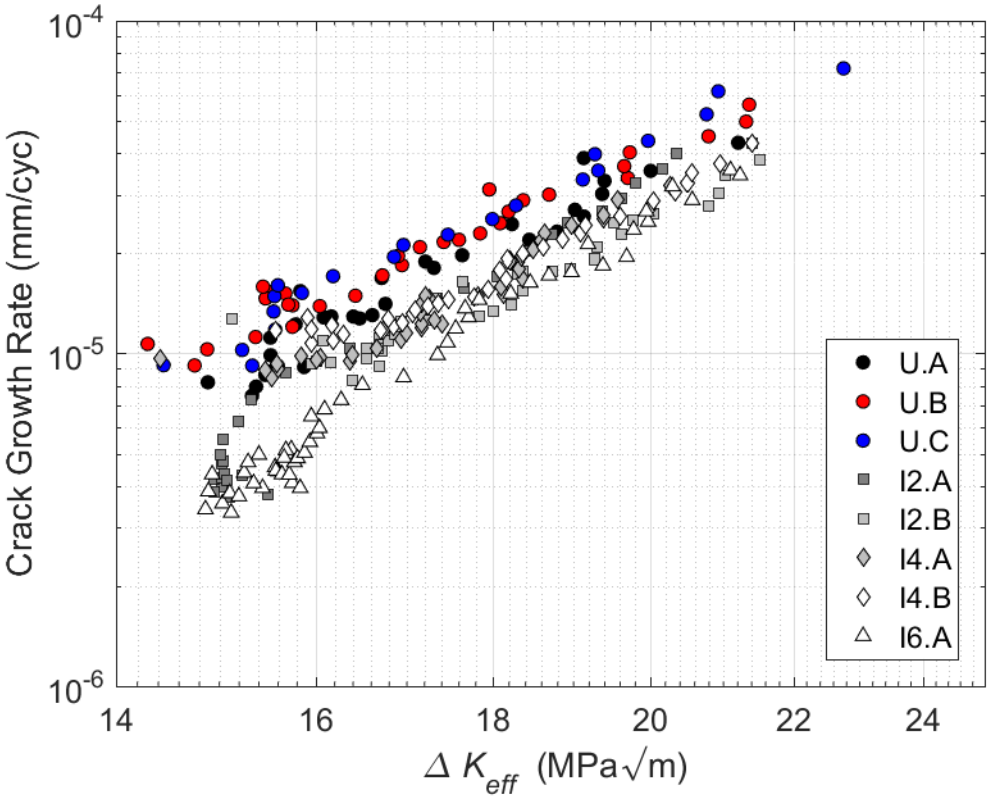

Figure 7 – Log-log plot of fatigue crack growth behaviour of unirradiated (filled circles) and irradiated specimens (see Table 2 for details).

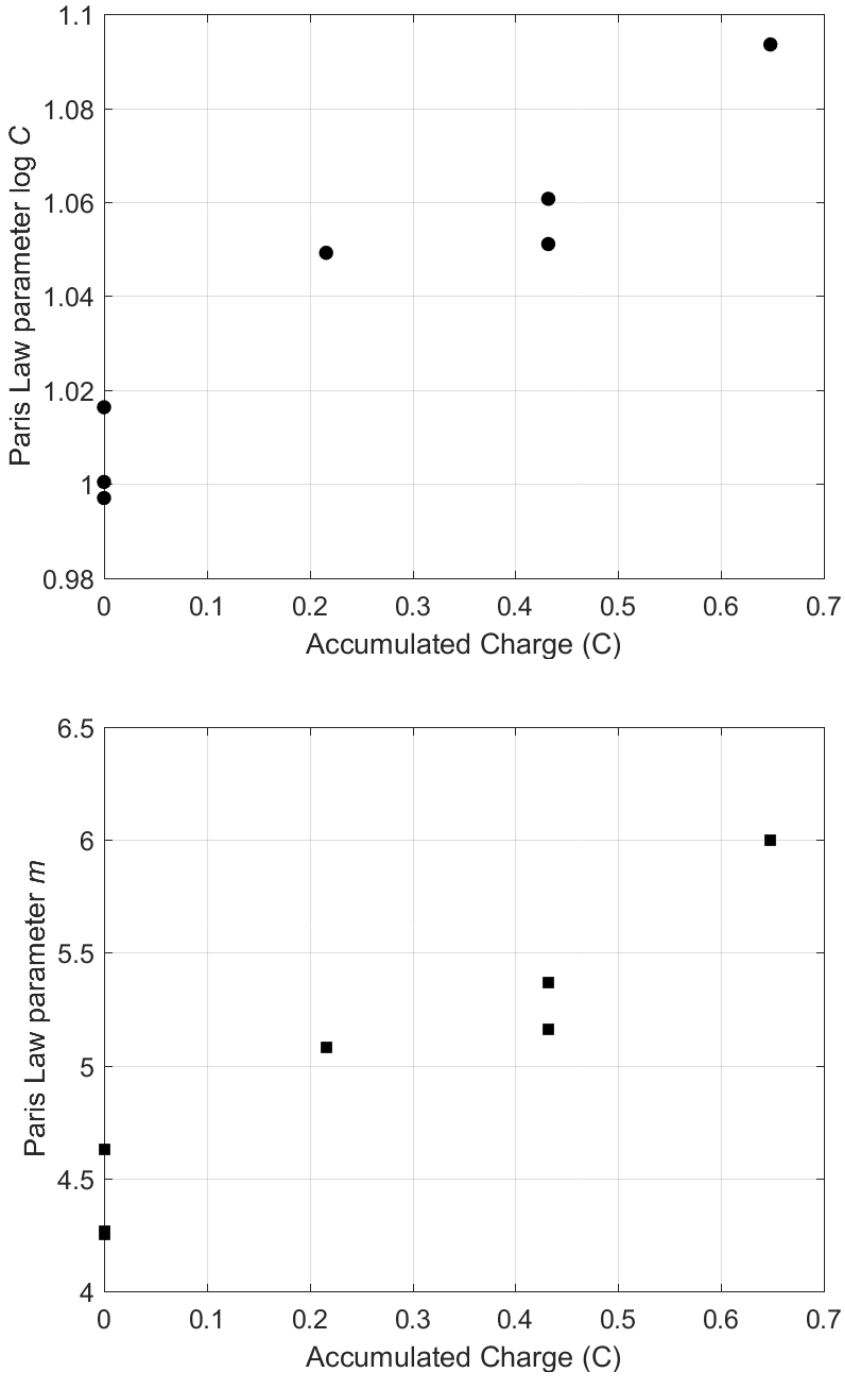

Figure 8 – Coefficients of the Paris law as a function of the irradiated damage characterised by the accumulated charge.